Compressibility Effects on Boundary-Layer Transition Induced by an Isolated Roughness Element

John A. Redford,* Neil D. Sandham,† and Graham T. Roberts‡
University of Southampton, Southampton, Hampshire SO17 1BJ, United Kingdom

Direct numerical simulation has been used to study the transition to turbulence of a high-speed boundary layer over a flat plate with an isolated roughness element. The roughness element consists of a continuous bump that is approximately half the boundary-layer thickness in height. Simulations at Mach 3 and Mach 6 have been run over a range of Reynolds numbers for two fixed wall temperatures corresponding to either an adiabatic or a cooled wall condition. In each case a lift-up of low momentum fluid away from the wall is observed leading to the formation of a detached shear layer. Acoustic disturbances are imposed to stimulate the instability of this layer and breakdown to turbulence is observed in the simulations at the highest Reynolds number in all cases except for the Mach 6 cold wall condition. The magnitude of the streamwise vorticity behind the roughness element increases with roughness height Reynolds number and is relatively insensitive to Mach number and wall temperature. Strouhal numbers associated with hairpin vortex formation are generally lower than in incompressible flow. The critical roughness height Reynolds number for transition within the computational domain is found to increase as the Mach number increases and is higher for the cooled wall condition. A correlation based on roughness height Reynolds and Mach numbers and wall temperature is found to separate laminar from transitional cases for the range of flow conditions studied.

Nomenclature

A, B	=	parameters in grid definition
a	=	sound speed
a_f	=	acoustic forcing amplitude
a_1, a_2	=	test case grid constants
C	=	Sutherland constant
C_f	=	skin-friction coefficient
C_n	=	constants ($n = 1, 2, 3$)
C_r	=	Chapman–Rubesin parameter
d	=	roughness element width
E	=	unsteady disturbance energy
E_T	=	total energy
f_n	=	acoustic forcing frequency increment
H	=	boundary-layer shape factor δ^*/θ
h	=	bump height
k	=	thermal conductivity
l_x, l_y, l_z	=	domain size
M	=	freestream Mach number
M_c	=	convective Mach number
M_h	=	roughness height Mach number $M_h = U_h \sqrt{\rho_h/(\gamma p_h)}$
N_f	=	number of acoustic forcing frequencies
N_x, N_y, N_z	=	number of grid points
Pr	=	Prandtl number
p	=	pressure
Re	=	Reynolds number based on freestream properties and inlet boundary-layer displacement thickness
Re_h	=	roughness height Reynolds number $\rho_h U_h h/\mu_h$
$Re_{\dot{x}_h}$	=	Reynolds number based on freestream properties and $\dot{x}_h$
R	=	radius of the acoustic source
r	=	distance from acoustic source
S	=	acoustic source strength
Sr	=	Strouhal number
T	=	temperature
T_w	=	wall temperature
T_∞	=	freestream temperature
t	=	time
U	=	streamwise mean velocity
u_i	=	velocity vector
u, v, w	=	velocity components
x, y, z	=	Cartesian coordinate system $\equiv x_i$
$\dot{x}_h$	=	streamwise distance from plate leading edge to roughness element
Y_j	=	grid stretching function
α	=	streamwise wavenumber
β	=	spanwise wavenumber
γ	=	ratio of specific heats c_p/c_v
δ	=	boundary-layer thickness $y(u \equiv 0.99 U_\infty)$
δ^*	=	boundary-layer displacement thickness $\int_0^\infty (1 - \rho u/\rho_\infty U_\infty)\,dy$
δ_0^*	=	inlet boundary-layer displacement thickness
δ_{ij}	=	Kronecker delta
μ	=	dynamic viscosity
ξ_i	=	coordinate in the computational domain
Π	=	second invariant of the velocity gradient tensor
ρ	=	fluid density
τ_{ij}	=	shear stress
ϕ_n	=	random phase angle sequence
ψ	=	amplitude of fluctuation
ω_i	=	vorticity

Subscripts

h	=	quantity taken at roughness height in unperturbed laminar boundary layer
i, j, k	=	tensor notation
r	=	reference condition, Eq. (16)
s	=	acoustic source location
0	=	inlet quantity
∞	=	freestream quantity
$\sim$	=	distance measured from the bump location

*Research Fellow, School of Engineering Sciences; j.a.redford@soton.ac.uk.
†Professor, School of Engineering Sciences; n.sandham@soton.ac.uk. Senior Member AIAA.
‡Senior Lecturer, School of Engineering Sciences; g.t.roberts@soton.ac.uk.

I.   Introduction

TRANSITION from laminar to turbulent flow in a boundary layer is important when trying to quantify surface heat transfer and drag for supersonic or hypersonic flight vehicles. Reshotko [1] notes five different routes through transition and gives particular attention to the occurrence of transient growth phenomena, which provide a link between the initial receptivity processes (by which disturbances enter the boundary layer) and the parametric instabilities that lead to the final breakdown to turbulence. This route to turbulence is particularly relevant to transition in flow over a rough surface. A comprehensive review of the current understanding of the effect of roughness on hypersonic boundary-layer transition has been recently published by Schneider [2]. He notes the complexity of the processes, the difficulties involved in carrying out laboratory experiments and the limitations of the correlations that are available for design applications. In contrast to many other areas of transition research, direct numerical simulations (DNS) have so far made only limited contributions to understanding transition due to surface irregularities in high-speed flows, at least in part due to the large computer resources that are needed to fully resolve the transition region. The objective of the present work is to demonstrate that such simulations are feasible and to use DNS to start exploring the large parameter space involved in hypersonic roughness-induced transition. To reduce the number of simulations we consider only isolated sub-boundary-layer roughness elements.

The Reynolds number is generally the most significant parameter in transition and it is well known [3] that a useful form of the Reynolds number for an isolated roughness element that is smaller than the boundary-layer thickness is

$$Re_h = \frac{\rho_h^* U_h^* h^*}{\mu_h^*} \qquad (1)$$

where h^* is the height of the roughness element and ρ_h^*, U_h^*, and μ_h^* are the fluid density, streamwise velocity, and dynamic viscosity at height h^* in the laminar boundary layer in the absence of the roughness element. (An asterisk is used here to denote a dimensional quantity but for the remainder of the paper we will work with dimensionless quantities.) At low Re_h the flow over the roughness element is steady, but beyond a critical Re_h (for example [4] found 325 for a hemispherical and 450 for a cylindrical element in incompressible flow) the roughness causes transition to turbulence. The critical value of Re_h is affected by the roughness shape [3,4], background disturbance levels [5], and compressibility [1]. An important parameter is known to be the roughness element aspect ratio d/h, where d is the roughness diameter and h is the roughness height. As shown in figure 22 of [2] for several roughness shapes, the critical Re_h decreases with d/h, appearing to asymptote to a value of about 300 for $d/h > 4$. The surface bumps considered in the present work will be in this category of high aspect ratio (i.e., shallow) roughness elements.

From experiments at low-speed we have a reasonable understanding of the physical mechanisms arising during roughness-induced transition. A roughness element distorts the flow in a laminar boundary layer, typically creating streamwise vorticity. Transient growth (lift-up) generates streaks and an unstable detached shear layer. Even if the boundary layer is already unstable, the larger instability caused by the shear layer usually accelerates the transition process. The growth of fluctuations within the detached shear layer is quick but for transition to be complete the high amplitude perturbations in this layer must penetrate into the near wall region and cause the formation of boundary-layer turbulence. The results of Klebanoff et al. [4] show that the shear layer perturbations may need to reach considerable strength before they have the ability to trigger boundary-layer turbulence. As pointed out by Ergin and White [5] the disturbed flow diffuses back to a more stable laminar boundary layer and whether or not transition occurs depends on whether the local instabilities can grow sufficiently strongly to trigger transition before they are stabilized. The flow in the vicinity of the roughness element is dependent on the shape of roughness and may contain areas of separation upstream and downstream of the roughness

element. Low-speed experiments most commonly use cylindrical or spherical roughness shapes, but other possible generic shapes are cubes and smooth bumps. It is known that the vortices surrounding the roughness element can be suppressed by a change in shape [6].

Acarlar and Smith [6] used dye and hydrogen-bubble-wire flow-visualization in their experiments on flow over a hemispherical roughness element. Under the correct conditions they observed that hairpin vortices were shed periodically from the roughness element. The hairpin vortices are a direct consequence of the lift-up mechanism that causes the formation of the detached shear layer. The instability within the shear layer causes a rollup that joins the trailing vortices. The instability has a characteristic frequency corresponding to the rate at which the hairpin vortices are formed. At high Reynolds number these hairpin vortices become turbulent, and the point at which this occurs fluctuates with the shedding of the hairpin vortices. The shear layer instability has a characteristic frequency f that can be nondimensionalized with a length scale and velocity to form a Strouhal number. The results of Acarlar and Smith [6] show that the Strouhal number increases quickly with Re_h at low values and then tends to asymptote to a constant value at high Re_h. Klebanoff et al. [4] also show this along with some dependence on shape. The frequency of shedding is important because it will play a part in determining the transition length. Klebanoff et al. [4] and Ergin and White [5] use the local boundary-layer displacement thickness (δ_h^*) and U_h to form the Strouhal number $Sr = f\delta_h^*/U_h$. At $Re_h = 334$ (i.e., beyond the critical value) Ergin and White measure $Sr = 0.15$ while Klebanoff et al. find Sr to be spread between 0.23 and 0.35 depending on the size of the roughness element.

Ergin and White [5] present detailed results for a spanwise array of cylindrical roughness elements of various heights covering sub- and supercritical cases. They observe lift-up and transient growth behind the elements in all cases, with increasing amplification of disturbances as Reynolds number is increased. In subcritical cases the fluctuations grow to a roughly constant level and remain within the outer part of the boundary layer. Beyond the critical Reynolds number, fluctuations spread throughout the boundary layer, especially into the near wall region causing the formation of boundary-layer turbulence. They conclude that a Kelvin–Helmholtz instability is active in the wake region behind the roughness elements.

Rizzetta and Visbal [7] have recently presented results from DNS of incompressible flow over a cylindrical roughness element at two Reynolds numbers based on roughness height, generally showing good agreement with the experiments of Ergin and White [5]. They found that the flow becomes turbulent downstream of the roughness element in their higher Reynolds number ($Re_h = 334$) case, with the formation of hairpin vortices during breakdown. In the low Reynolds number ($Re_h = 202$) case the simulation resolved two steady vortices wrapped around the cylindrical roughness element.

Most research has covered the incompressible case but differences in the transition process are known to occur in compressible flow. The critical Reynolds number caused by a roughness element appears to have some dependency on Mach number. Schneider [2] shows results suggesting that above Mach 4 there is a large increase in critical Reynolds number. However the high Mach number results were taken from [8] where only roughness elements greater than the boundary-layer thickness were tested. At high Mach numbers acoustic disturbances will be prevalent, particularly in enclosed wind-tunnel experiments [2]. Balakumar's [9] simulations show that a Mach 3.5 boundary layer is highly receptive to acoustic disturbances. Although his simulations with a roughness element failed to show enhanced receptivity it should be noted that the roughness was two-dimensional and very small. Marxen and Iaccarino [10] also simulated compressible flow over a two-dimensional roughness and liken the flow to a shock-wave boundary-layer interaction, in the sense that the roughness disrupts the instability waves that are already present in the flow. Groskopf et al. [11] consider the biglobal instability of the crossflow behind square-section roughness elements in a Mach 4.8 boundary layer. They find both span-symmetric and span-antisymmetric modes with generally similar growth rates. A similar biglobal analysis for incompressible flow by Piot et al. [12] showed a stabilizing effect of the roughness-induced

vortices. In supercritical cases, the fully turbulent wedge-shaped region downstream of an isolated roughness element is also expected to be sensitive to compressibility effects, since at higher Mach numbers it is known that turbulent spots have lower growth rates and a greater Reynolds number is required for the initial breakdown to occur [13–15].

In this article we use DNS to simulate an isolated roughness element represented by a smooth sub-boundary-layer bump. Given the difficulties inherent in experimental work summarized in [2] and the particularly limited database for cooled walls, it is of interest to see how DNS can be used to fill in some gaps in our understanding. The advantages of DNS include the ability to control the disturbance environment and then access the full three-dimensional flow field. The disadvantage is the computational cost. Here we confine ourselves to a limited study of the parameter space, including variations in Mach number, wall temperature and Reynolds number, with a total of 12 simulations. The general arrangement for the simulation is shown in Fig. 1. The computational domain includes an isolated roughness element and acoustic forcing. In Sec. II we present the method and discuss validation and grid refinement, highlighting some issues that occur when the disturbance environment is left to the numerics. In Sec. III we use controlled disturbances to examine the physical mechanisms of transition and in Sec. IV we collect the data together to give a correlation that separates transitional from laminar cases for the parameter range studied.

II. Method

A. Governing Equations and Code Verification Exercise for Nonorthogonal Meshes

The governing equations are the compressible Navier–Stokes equations for a Newtonian fluid with Fourier heat conduction. Variables are made dimensionless using the inlet displacement thickness and freestream velocity, temperature, density and viscosity, leading to

$$\frac{\partial \rho}{\partial t} + \frac{\partial \rho u_j}{\partial x_j} = 0 \tag{2}$$

$$\frac{\partial \rho u_i}{\partial t} + \frac{\partial \rho u_i u_j}{\partial x_j} = -\frac{\partial p}{\partial x_i} + \frac{1}{Re}\frac{\partial \tau_{ij}}{\partial x_j} \tag{3}$$

$$\frac{\partial E_T}{\partial t} + \frac{\partial (E_T + p)u_j}{\partial x_j} = \frac{1}{Re}\frac{\partial u_i \tau_{ij}}{\partial x_j} + \frac{1}{(\gamma - 1)RePrM^2}\frac{\partial}{\partial x_j}\left(\mu\frac{\partial T}{\partial x_j}\right) \tag{4}$$

where t is time, x_i is a Cartesian coordinate system, ρ is the fluid density, u_i is the velocity vector, $E_T = p/(\gamma - 1) + \rho u_i u_i/2$ is the total energy, and p is the pressure, which is related to the density and temperature T by the dimensionless form of the perfect gas law $T = \gamma M^2 p/\rho$, where γ is the ratio of specific heats and is set to 1.4. Re is the reference Reynolds number, M is the freestream Mach number and the Prandtl number $Pr = 0.72$. The shear stress tensor is given by

$$\tau_{ij} = \mu\left(\frac{\partial u_j}{\partial x_i} + \frac{\partial u_i}{\partial x_j} - \frac{2}{3}\delta_{ij}\frac{\partial u_k}{\partial x_k}\right) \tag{5}$$

where viscosity is calculated using Sutherland's law $\mu = T^{3/2}(1 + C)/(T + C)$ where $C = 110/288$ corresponds to a Sutherland constant of 110 K and a reference temperature of 288 K. In our formulation this Sutherland reference temperature is the same as the inflow reference temperature. The nonpower law variation of viscosity with temperature means that in principle different simulations have to be run to match different experimental or flight conditions for freestream temperature. Here we take standard conditions.

Derivatives are computed using fourth-order centered finite differences and the time integration is carried out using a third-order low-storage Runge–Kutta method. The stability of the calculation is improved by the use of entropy splitting [16,17]. Since the flow over a roughness element was found to generate a shock wave, a shock capturing method [16] was employed for all these cases.

The current problem requires a grid to be fitted to a curved surface for which a three-dimensional metric transformation [18] is necessary. This transforms a regularly spaced grid in computational space ξ_i suitable for mapping finite differences to an arbitrary grid in the Cartesian coordinate system x_i

$$\frac{\partial}{\partial x_n} = \frac{\partial}{\partial \xi_m}\frac{\partial \xi_m}{\partial x_n} \tag{6}$$

$$\frac{\partial}{\partial x_n}\left(\frac{\partial}{\partial x_o}\right) = \frac{\partial \xi_l}{\partial x_n}\left[\frac{\partial \xi_k}{\partial x_o}\frac{\partial^2}{\partial x_k \partial x_l} + \frac{\partial}{\partial \xi_l}\left(\frac{\partial \xi_k}{\partial x_o}\right)\frac{\partial}{\partial \xi_k}\right] \tag{7}$$

At the start of the simulation the metric terms $\partial \xi_i/\partial x_j$ and $\partial/\partial \xi_i(\partial \xi_j/\partial x_k)$ are calculated numerically using Eqs. (6) and (7), and stored.

At the inlet we use a similarity solution for a compressible boundary layer to prescribe profiles of density, velocity and temperature. At the top and outflow boundaries, characteristic boundary conditions are applied to reduce the reflection of waves back into the domain. Periodic boundary conditions are used in the lateral direction, meaning that we have a periodic array of identical roughness elements. However, the simulations were set up with a wide enough domain such that the roughness elements are essentially isolated.

The code was verified by running the linear stability test case described in [19], in which the growth rate of a Mack mode of instability in a Mach 6 boundary layer is computed using a temporal simulation. The problem is two-dimensional and a grid with $N_x = 32$ and $N_y = 251$ points, with dimensions $l_x = 3$ and $l_y = 8$ was used. Grid stretching is used to place points near the surface and grid curvature is introduced to test the metric transformation using

$$x = x_i + a_1 \sin(2\pi z_k/l_y) \tag{8}$$

$$z = z_k + a_2 \sin(2\pi x_i/l_x)\sin(\pi z_k/l_y) \tag{9}$$

where $x_i = i/N_x l_x$, $z_k = l_y \sinh(C_1(k-1)/(N_y - 1))/\sinh(C_1)$, $k = 1, 2, \ldots, N_y$, and $C_1 = 2.5$. The parameters a_1 and a_2 are used to control the amount of grid skewing. The disturbance growth is tracked by calculating the time variation of the root mean square of the normal velocity, integrated over the computational domain. An example where the perturbation strength is calculated using $\psi(t) = \int_0^2 \sqrt{\overline{v'^2}}\,dy$ is shown on Fig. 2 for grid 1, and the calculated growth rates $d\ell_n(\psi)/dt$ are shown on Table 1 for each grid studied. For the first two cases the predictions from the code and the Orr–Sommerfeld solver match within 0.2%. The errors increase with grid skewing, but show good agreement for moderate levels of grid skew.

B. Bump Geometry and Grid Generation

For the DNS calculations, the domain sizes in the streamwise, vertical and lateral directions are set to $l_x = 325$, $l_y = 16$, and
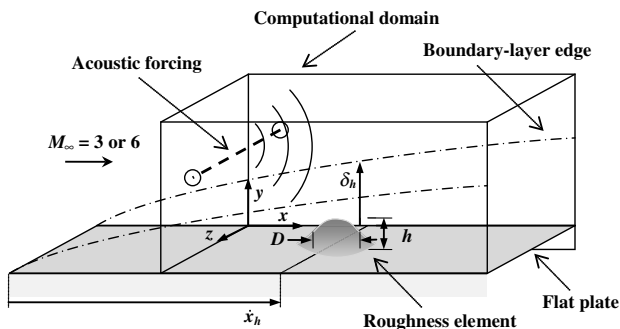

Fig. 1 A schematic showing the major features of the simulation, and relation between the simulation and experimental flow.
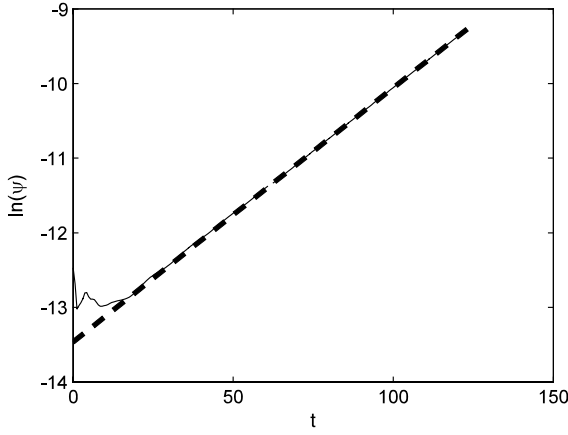
Fig. 2 Growth of a boundary-layer perturbation. Variation of amplitude with time including dashed line with slope $d \ln(\psi)/dt = 3.4088 \times 10^{-2}$.

$l_z = 64$, respectively. The bump is positioned at $x_h = 125$ and $z_h = 32$ with a smooth surface contour prescribed by

$$y = -A\left(\tanh\left(\frac{\sqrt{\tilde{x}^2 + \tilde{z}^2}}{B} - 1 \right) + \tanh\left(-\frac{\sqrt{\tilde{x}^2 + \tilde{z}^2}}{B} - 1 \right) \right) \quad (10)$$

where $\tilde{x} = x - x_h$ and $\tilde{z} = z - z_h$ are coordinates relative to the center of the bump. The constants are set as $A = 0.855$ and $B = 2.56$. Figure 3 shows the bump, which has a height of $h = 1.3$, a half-width of 6.24 (i.e., the diameter of the bump when $y = h/2$) and $d/h = 5.2$, along with part of the computational grid. For accurate solution of the flow great care needs to be taken with the grid generation. The grid for the current geometry was based on analytic functions and adapted to reduce skewing of grid cells, while having sufficient points to achieve a good resolution. The grid, with $N_x \times N_y \times N_z$ points, was generated by first of all creating a series of surfaces y_j ($j = 1, 2, \ldots N_y$)

$$y_j = -A_j\left(\tanh\left(\frac{\sqrt{\tilde{x}^2 + \tilde{z}^2}}{B_j} - 1 \right) \right.$$
$$\left. + \tanh\left(-\frac{\sqrt{\tilde{x}^2 + \tilde{z}^2}}{B_j} - 1 \right) \right) + Y_j \quad (11)$$

A stretching function was applied to Y_j to place more points near the surface according to

$$Y_j = l_y \sinh\left(C_1 \frac{j-1}{N_y - 1} \right) / \sinh(C_1) \quad (12)$$

where the function constant is $C_1 = 2.5$ and $j = 1, 2, \ldots N_y$. At points further from the surface the contour of the bump is gradually reduced so that the top surface is flat using

$$A_j = \frac{C_2}{2}\left(1 + \cos\left(\frac{j}{N_y} \pi \right) \right) \quad (13)$$

with $C_2 = 0.855$. To prevent an accumulation of points in the freestream the bump shape is spread using the function
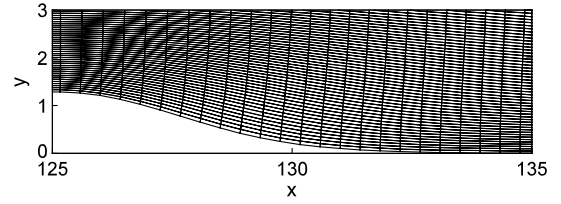
Table 1 Growth rates and errors for the stability test

Case	Growth rate $d \ln(\psi)/dt$	Error %	a_1	a_2
Orr–Sommerfeld	3.4134×10^{-2}	——	——	——
Grid 1	3.4088×10^{-2}	-0.13	1	0.05
Grid 2	3.4120×10^{-2}	-0.04	2	0.05
Grid 3	3.3754×10^{-2}	-1.1	1	0.1
Grid 4	3.2886×10^{-2}	-3.7	1	0.25

Fig. 3 Computational grid over the roughness element at $z = 32$ (centerline).

$$B_j = C_3\left(1 + C_4 \frac{j-1}{N_y - 1} \right) \quad (14)$$

where $C_3 = 2.56$ and $C_4 = 6$. On the lower surface ($j = 1$) the grid is uniformly spaced in x and z. The x, y and z points at subsequent levels $j > 1$ are found by projection outwards along the unit normal vector added to a vertical vector of length 0.8. Combining with the vertical vector provides a more even spread of points in the freestream. An example of a grid created in the vicinity of the bump is shown in Fig. 3. Further from the bump the grid curvature becomes small such that at the lateral extremities of the domain the grid is orthogonal, allowing periodic boundary conditions to be satisfied.

C. Acoustic Forcing

Most boundary-layer flows are convectively unstable and need to be fed with suitable upstream fluctuations. Fluctuations are often present in numerical simulations at some level due to the limited spatial or temporal resolution but it is usually preferable to perturb the flow in a controlled way rather than rely on this numerical noise as the trigger for transition. Perturbations can be introduced within the boundary layer itself or via the freestream, from where they enter the boundary layer by a receptivity process. Several methods, including the direct input of random perturbations within the boundary layer, were tested in the present study, but it was found that the most effective method was to introduce the disturbance within the free-stream in the form of an acoustic line source placed a short distance upstream of the bump. This experience mirrors that of experiments at high Mach number [2] where transition is highly dependent on acoustic radiation from sidewall boundary layers. A range of frequencies are used, with the maximum frequency being designed such that it is resolved by about 15 grid points per wavelength in the worst case. Each frequency is given a random phase angle to prevent spurious peaks from arising. The spatial and time dependence of the acoustic source are combined using

$$S(r, t) = \frac{a_f}{2}\left[1 - \cos\left(\pi\left(1 - \frac{r}{R} \right) \right) \right] \sum_{n=1}^{N_f} \sin(2\pi f_n nt + \phi_n) \quad (15)$$

which is added to the right hand side of Eq. (2) with an amplitude $a_f = 1/80$ at Mach 3 and $1/320$ at Mach 6. A total of $N_f = 8$ frequencies in increments of $f_n = 0.02$ were used with phase angles ϕ_n set as random numbers between 0 and 2π. The acoustic line source is introduced when $r < R$ where the radial distance from the center of the acoustic source is $r^2 = (x - x_s)^2 + (y - y_s)^2$, and the radius of the acoustic source is $R = 1$.

The acoustic source is first tested on a two-dimensional flat plate boundary layer without a roughness element in a domain of size $l_x = 325$ and $l_y = 16$. The source is located at $y_s = 8$, with $x_s = 101$ at Mach 3 and $x_s = 77$ at Mach 6. An example of the Mach 3 adiabatic wall condition in Fig. 4a shows that the acoustic disturbance spreads within a region enclosed by the Mach angle. The disturbance impacts on the boundary layer and reflects back into the freestream. The characteristic boundary condition at the top of the domain successfully absorbs both the direct and surface-reflected waves. From Fig. 4b, it can be seen that the streamwise velocity perturbations in the boundary-layer peak just upstream of the intended roughness location ($x_h = 125\delta_0^*$) and then reduce to a root-mean-square value of about 0.2% of the freestream velocity further downstream. The perturbation is growing toward the end of the
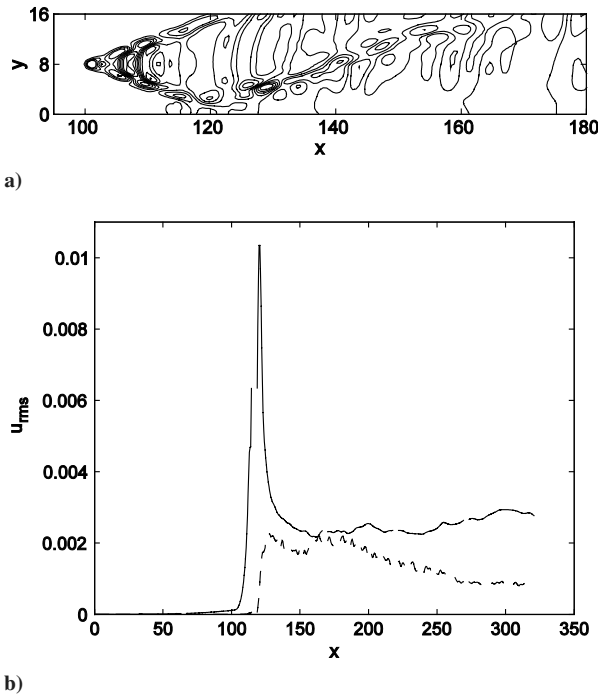
a)

b)

Fig. 4 Schematic a) instantaneous pressure contours when acoustic disturbance is introduced to a flat plate flow with $Re_{\delta_0^*} = 2250$, $M = 3$ and $T_w = 2.517$, using $N_x = 624$ and $N_y = 120$ grid points. Contours of p/p_∞ starting at 0.92 and increase in increments of 0.01. Schematic b) maximum fluctuation velocity within the boundary layer ——, and along the top of the domain – – –.

domain because the boundary layer is unstable ($Re_{\delta_0^*}$ is greater than the critical value given in Table 2), but the growth is weak and the perturbations are still small at the domain outlet.

Simulations similar to that shown in Fig. 4 have been run for a range of Reynolds and Mach numbers. The disturbance level only has a weak dependence on the Reynolds number and wall temperature, but the increased Mach number results in a significantly larger perturbation within the freestream (above the bump at $M = 3$ $p_{rms}/p_\infty = 0.8 \times 10^{-2}$ and at $M = 6$ $p_{rms}/p_\infty = 1.8 \times 10^{-2}$) and in the boundary layer. However, in each case the perturbations are too small to trigger transition by themselves, requiring the introduction of a roughness element to achieve transition to turbulence.

D. Grid Dependence Study of Forced and Unforced Cases

To test the resolution a case at Mach 3 with a wall temperature equal to the adiabatic wall temperature has been simulated on five grids, details of which are given in Table 3. Relatively small increments in grid size are used since convergence is expected to be rapid for the high-order methods used. For comparison, the finest grid from Rizzetta and Visbal [7] was $713(x)$ by $201(y)$ by $155(z)$. Figure 5 shows each of the unforced simulations at a time instant after initial transients have passed out of the domain. At the lowest resolution the shear layer breaks up early due to an instability wavelength that is close to the grid spacing. Increasing the resolution causes the initial instability location to move further downstream and for the finest grid there is no breakdown to turbulence and the flow relaxes slowly back to a laminar solution. Clearly the unforced case has an undesirable grid dependency. Figure 6 shows the same tests

carried out with acoustic forcing. In this case a shear layer instability is clearly visible and consistent results are obtained between the simulations using grids C to E.

The skin-friction coefficient is defined as $C_f = \tau_{12}|_w / \frac{1}{2}\rho_\infty U_\infty^2$ where $\tau_{12}|_w$ is the wall shear stress. A correlation for flat plate skin-friction coefficient can be found for laminar compressible flow using the method given by Eckert [20]. First, recalling briefly that temperature and viscosity are normalized with their freestream values, a reference condition is calculated within the laminar boundary layer

$$T_r = \frac{1}{2}(1 + T_w + 0.22\sqrt{Pr}(\gamma - 1)M^2) \quad (16)$$

and a Chapman–Rubesin parameter is defined as $C_r = \mu_r\rho_r$. Note that the boundary-layer reference temperature T_r is not to be confused with the reference temperature used in the Sutherland viscosity law. A laminar skin-friction approximation is given by $C_f = 0.664/\sqrt{Re_x/C_r}$. Figure 7, a plot of the streamwise distribution of skin friction, shows some grid dependency of C_f for coarse grids. Before the flow becomes turbulent the simulations agree well, firstly up to $x = 90$ where the laminar flat plate correlation is followed accurately, then ahead of the bump there is separation ($C_f < 0$), followed by accelerated flow (high C_f) over the top of the bump and then separation again downstream of the bump. Grids C–E with acoustic forcing all show a peak in skin friction of a similar magnitude at the streamwise location where vortical structures impact on the surface (near $x = 240$ in Fig. 6). In this case the start of transition, indicated by the rapid rise in skin friction downstream of the immediate vicinity of the bump, is taken to occur at $x \approx 180$, and the simulations using grids C–E could all be used to predict this point. In the unforced case there is no such rise in skin friction, and although the skin friction is greater than that of the flat plate because of the presence of the bump, the flow remains laminar.

E. Overview of Simulations with Acoustic Forcing

A set of simulations were run with freestream Mach numbers of 3 and 6 with the wall temperature set to either the laminar adiabatic wall temperature or equal to the freestream temperature (i.e., a cooled wall condition). Flow parameters are shown in Table 4. A range of Reynolds numbers were used, sufficient to capture a critical Reynolds number for transition in all the cases except the Mach 6 cold wall condition, which remained laminar up to the highest roughness Reynolds number studied. The stability of the laminar base flow was calculated by solving the compressible Orr–Sommerfeld equation. Table 2 shows the critical Reynolds number, which was found by varying the streamwise (α) and spanwise (β) wavenumbers to find the minimum Reynolds number for neutrally stable disturbances. The table includes the values of α and β. It can be seen that the critical Reynolds number occurs for two-dimensional waves in all cases except for the $M = 3$ hot wall case. Comparing the results in Table 2 with the data in Table 4 we can see that the laminar boundary layer without roughness is stable ($Re_{\delta_0^*}$ is less than the critical value) in the Mach 3 cold wall case and unstable in all other cases.

The same bump geometry was used for each simulation. Differences in the flow conditions mean that there are variations in δ_h^*/h (the displacement thickness of the undisturbed boundary layer at the bump location) from 0.9 to 2 (Table 4). Along with the roughness height Reynolds number defined by Eq. (1), a roughness Mach number $M_h = U_h\sqrt{\rho_h/(\gamma p_h)}$ is shown in the table. Each case was

Table 2 Laminar base flow instability data

M	T_w	Critical Re_{δ^*}	α	β
3	2.517	1056	0.30	0.41
3	1	3682	1.66	0
6	7.027	2250	1.93	0
6	1	726	1.19	0

Table 3 Computational grid sizes

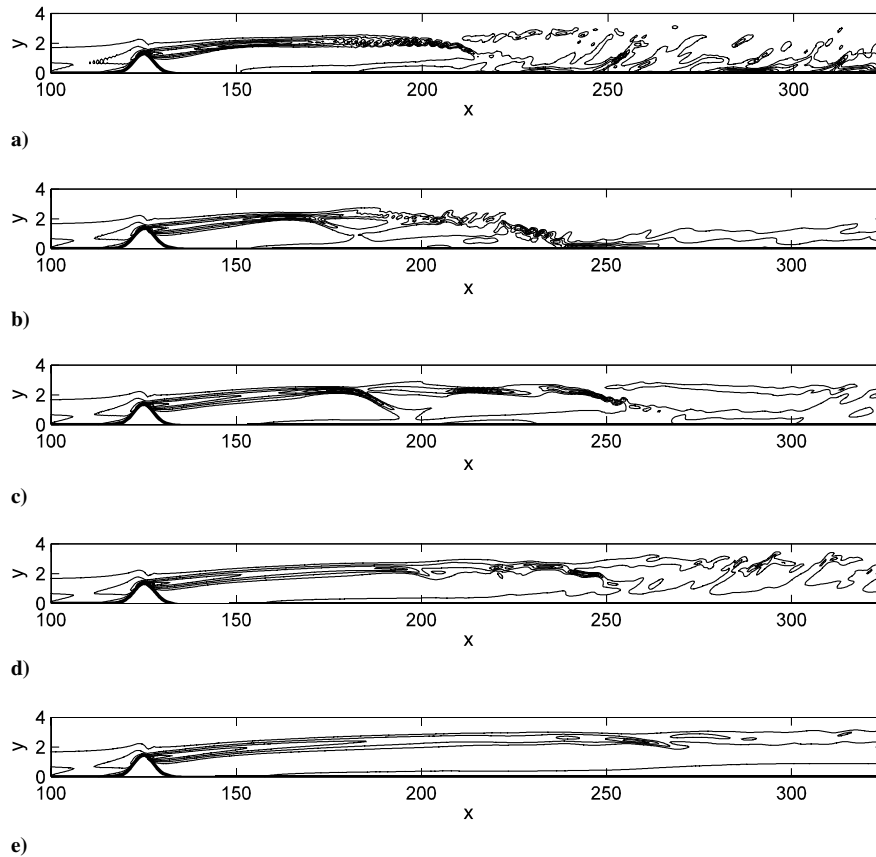| Grid	N_x	N_y	N_z
A	624	120	120
B	780	150	150
C	936	180	180
D	1092	180	210
E	1248	210	240

Fig. 5   Contours of shear stress starting at $\tau_{12} = 0.5$ and increasing in increments of 0.5 along the domain centerline for case Hot3B (see Table 4). Five increasingly well-resolved cases: a) grid A, b) grid B, c) grid C, d) grid D, and e) grid E. The vertical axis is stretched by a factor of 4.

initially run using grid B (see Table 3) to gain an impression of the parameter space. In cases where transition occurred the resolution was increased (typically up to grid E) until the results were consistent.

Figure 8 gives an overview of the computational results, showing a plan view of the streamwise velocity perturbation for three cases that show transition to turbulence. The flow behind the roughness element is initially laminar with streaks developing in the velocity field. Along the centerline there is initially a negative velocity perturbation, indicating the lift-up of low-speed fluid from near the wall. Either side of this there are regions with a higher velocity than the unperturbed laminar boundary layer, where high-speed fluid is pushed toward the wall. Together with the observation of lift-up, this implies the presence of streamwise vortices in the flow. Starting from the region of lift-up, fluctuations grow and eventually cause a breakdown to turbulence, increasing the lateral spreading of the wedge of disturbed fluid behind the roughness element. In the next section we consider in more detail the mechanisms that lead to breakdown and how these are affected by changes in Mach number and thermal wall boundary condition.

III.   Mechanism of Breakdown to Turbulence

A.   Flow over the Roughness Element

The roughness elements protrude sufficiently into the flow to cause expansion and shock waves to form in the supersonic free-stream. Figure 9a shows the pressure distribution at the surface (solid line) and in the freestream (dashed line) for case Hot3B (defined in Table 4), while Fig. 9b shows corresponding pressure contours along the domain centerline. Variations in the inlet Reynolds number, Mach number and wall temperature change the strength of pressure perturbations but the basic wave pattern remains the same in other cases. There is a compression wave in front of the bump which can coalesce to form a shock wave at high M and low T_w, followed by an expansion and then a recompression shock. The latter originates from

the downward-sloping face of the roughness element close to the location of boundary-layer separation. The pressure waves created by the isolated roughness element are conical and their strength diminishes more rapidly away from the wall than would be the case for a two-dimensional bump.

An obstacle placed within the boundary layer introduces streamwise and lateral velocity gradients and an associated vorticity generation by a mechanism of stretching and convection. When the boundary layer is thin compared with the object one typically finds a necklace vortex wrapping around the object, with a downflow region immediately behind the object. This is not the case in the present configuration where the bump is smooth and immersed in the boundary layer. Figure 10 shows two perpendicular views of three particle trajectories calculated from a single velocity field, which is representative because the flow in this region is steady to a good approximation. As the flow approaches the roughness element it is displaced upward and away from the centerline. The fluid that starts at $y = 0.5$ (the solid line) passes the roughness element and is suddenly pushed upward behind the roughness element, while the fluid that starts at $y = 1$ near the domain centerline (the dash-dotted line) passes over the top of the roughness element and only slightly changes its height. By contrast, a particle that starts further away from the bump centerline (at $y = 1$, dashed line) is pushed nearer the wall. These particle trajectories illustrate the process of lift-up that leads to the formation of the velocity streaks seen in Fig. 8. In Fig. 10b it is possible to see how the fluid is tending to rotate about an axis oriented in the streamwise direction after it has passed the roughness element. The streamwise structure of corotating vortices is clearly visible in isosurfaces of the second invariant of the velocity gradient tensor $\Pi = (\partial u_i / \partial x_j)(\partial u_j / \partial x_i)$ as shown on Fig. 11. It is strongest just behind the roughness element and reduces in strength further downstream. An additional structure is present on the top of the bump, where the rotation rate seems to be directly related to the bump curvature. Contrary to [4,10] we only see one clear streamwise vortex pair. The difference is possibly due to the cylindrical geometry used
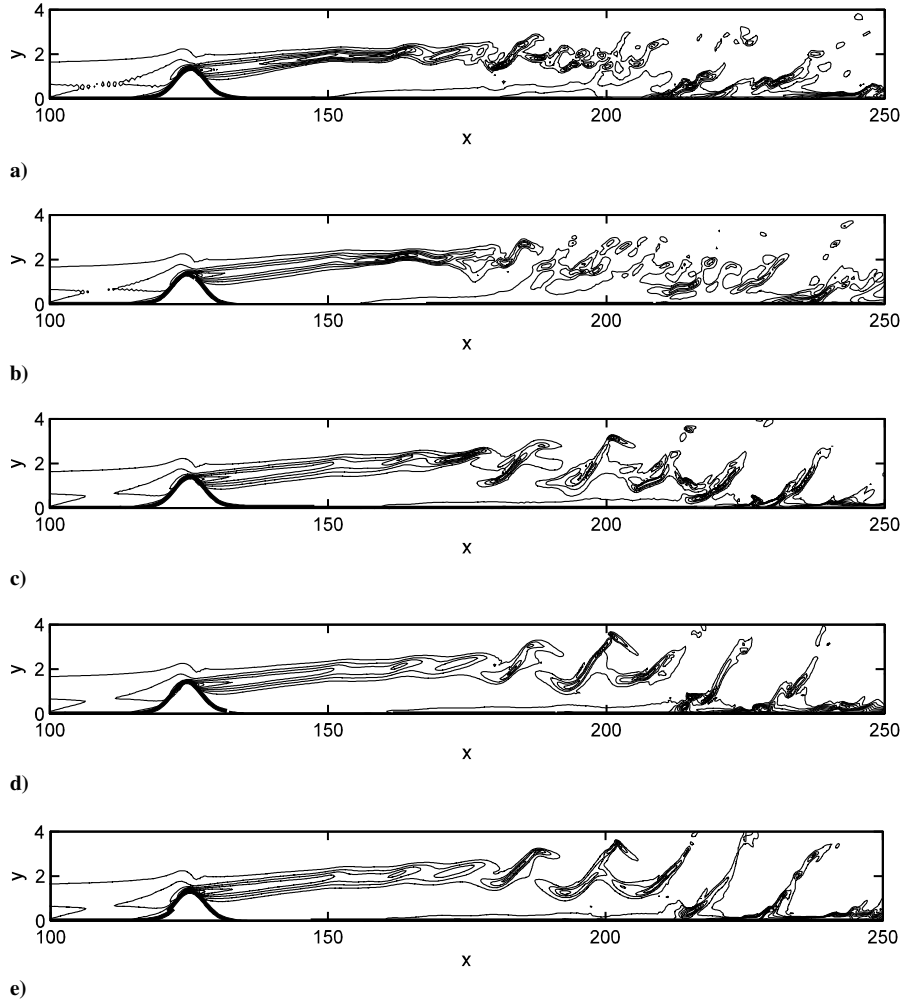
Fig. 6   Contours of shear stress starting at $\tau_{12} = 0.5$ and increasing in increments of 0.5 along the domain centerline for case Hot3B (see Table 4) with acoustic forcing. Five increasingly well-resolved cases: a) grid A, b) grid B, c) grid C, d) grid D, and e) grid E. Times chosen at the same point in the forcing cycle. The vertical axis is stretched by a factor of 4.

in those experiments and simulations compared with the smooth bump used here. The cylinder flows contain a weak necklace vortex in addition to the vortex pair seen here. There is also a difference to the Piot et al. [12] shallow bump flow (i.e., with a very high bump aspect ratio $d/h = 33.7$), which showed pairs of vortices at the bump edges with a wide space in between with no vortex structures. Clearly
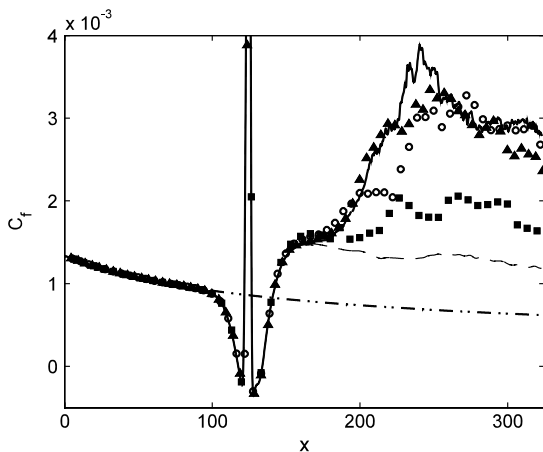
the flow pattern is sensitive to the detailed shape of the roughness. The present shape appears to be very effective in generating a strong streamwise vortex pair behind the element.

Figure 12 shows crossflow velocity vectors and streamwise vorticity and confirms the presence of a streamwise vortex pair for three different Reynolds numbers of the Mach 3 hot wall case. The maximum streamwise vorticity is located at about a half to two-thirds of the bump height, moving nearer to the wall as Re_h increases. The maximum streamwise vorticity is plotted on Fig. 13 for all the simulations. Note that in this and subsequent figures we denote cases that remain laminar with open symbols and cases that undergo transition to turbulence with closed symbols. It can be seen that all the cases follow a similar increasing trend with Re_h. The effects of Mach number and wall thermal condition are secondary to those of Re_h.

B.   Shear Layer Formation and Instability

The immediate consequence of the relative lift-up of fluid particles from lower in the boundary layer is that a detached shear layer is formed, as illustrated by contours of $\partial u/\partial y$ in the crossflow plane on Fig. 14a. The figure also shows the increased wall friction either side of the bump ($z = 30$ and $z = 34$) that was seen as high-speed streaks on Fig. 8. A vorticity stretching mechanism for formation of such shear layers was first elucidated by Stuart [21] and is well understood; see for example the application to shear layer formation and subsequent breakdown in plane channel flow in [22]. Figure 14b shows the presence of lateral shear layers $\partial u/\partial z$, which can have an effect on the breakdown mechanism [23] but are weaker than the $\partial u/\partial y$ component in the present simulations. To quantify the

Fig. 7   Case Hot3B (see Table 4) skin-friction coefficient with grid B (filled squares), grid C (circles), grid D (filled triangles), and grid E, averaged over a band of $z = z_c \pm 2.1$. — · · — is the Eckert [20] correlation for laminar flow – – – is for grid E without acoustic forcing.

Table 4   Flow case descriptions

Case	T_w	M	$Re_{\delta_0^*}$	$Re_{x_h} \times 10^5$	Re_h	M_h	δ_h^*	H	δ_h	Transition	Grid
Hot3A	2.517	3	1500	2.8	324	1.2	1.8	8.4	2.9	N	B
Hot3B	2.517	3	2250	4.8	595	1.4	1.6	8.4	2.5	Y	E
Hot3C	2.517	3	3000	7.3	920	1.5	1.4	8.4	2.3	Y	E
Cold3A	1	3	1100	3.0	561	1.7	1.3	7.8	2.9	N	B
Cold3B	1	3	1500	5.0	820	1.8	1.3	7.8	2.8	Y	D
Cold3C	1	3	1750	6.4	985	1.8	1.2	7.8	2.7	Y	E
Hot6A	7.027	6	4000	6.0	117	1.1	2.6	25	3.1	N	B
Hot6B	7.027	6	8000	14	440	1.7	1.9	25	2.3	Y	D
Hot6C	7.027	6	9500	17	620	1.8	1.8	25	2.2	Y	E
Hot6D	7.027	6	11000	21	810	2.0	1.7	25	2.1	Y	E
Cold6A	1	6	3000	6.9	774	3.1	1.5	8.9	2.3	N	B
Cold6B	1	6	3500	8.7	975	3.2	1.5	8.9	2.2	N	D

strength of the main shear layer, Fig. 15 shows the peak velocity gradient $(\partial u / \partial y_{\max})$ in the detached shear layer immediately downstream of the bump. In all cases the shear layer strength increases with Re_h. The shear layer is weaker in the Mach 6 cold wall case by a greater factor than for the vorticity field (Fig. 13), reflecting the sensitivity of the vorticity stretching mechanism to the flow conditions.

An indication of the effect of compressibility on the instabilities developing in the detached shear layer can be obtained from the convective Mach number $M_c = (u_1 - u_2)/(a_1 + a_2)$, where the subscripts 1 and 2 are measurements taken above and below the shear layer. An estimate of M_c has been made at $x = 150$ where the top and bottom of the shear layer are either side of the lowest contour plotted in Fig. 6e, and from similar plots at different Mach numbers and wall temperatures. The values of M_c are around 0.8 to 0.9 for the Hot3B, Cold3C and Cold6B cases and 1.2 for the Hot6C case. Instability growth rates compared with incompressible flow are around a factor of 2 lower at $M_c = 0.6$, and a factor of 3 lower at $M_c = 1.0$ [24]. Thus, the shear layers seen behind the roughness elements are all strongly affected by compressibility, with the largest effect expected for the Hot6C case.

The detached shear layer instability is of a convective nature, since in the absence of physical or numerical noise (cf. the grid refinement study in the absence of acoustic forcing) the flow remains laminar and the shear layers gradually diffuse back into the laminar boundary layer. This is not to say that in some cases the instability near the roughness element might be absolute in nature, as pointed out by Marxen and Iaccarino [10]. An indication of the possibility that the flow is absolutely unstable can be seen in the length of separation. Large separated regions would be a source of absolute instability. The lengths (Δx_s) of the reverse flow regions (where $C_f < 0$ along the bump centerline) upstream and downstream of the bump are shown in Fig. 16; when there is no separation the length is marked as $\Delta x_s = 0$. In all cases except Cold6B the separation is longest downstream of the bump. The separation is almost completely suppressed in the Mach 6 cold wall case. Other than this extreme case the length of separation in front of the bump increases slowly with Re_h, while the downstream separation seems to be affected by Mach number and wall temperature as well as Re_h. For the Mach 6 hot wall the downstream separation length is still increasing with increasing Re_h, while the Mach 3 cases already seem to have reached their maximum separation lengths. Although the roughness element
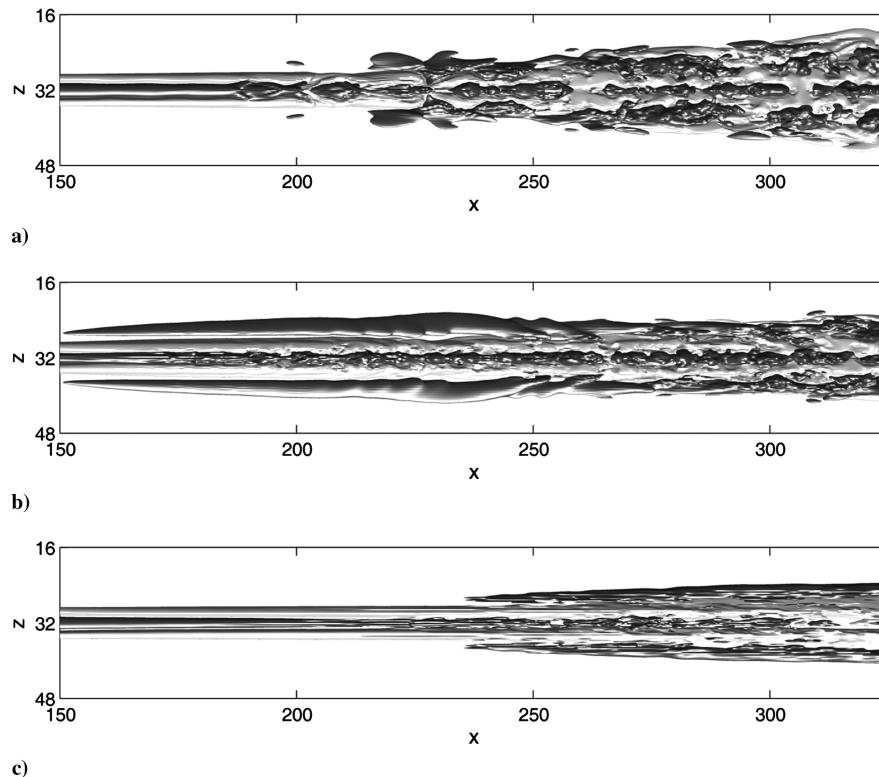

a)

b)

c)

Fig. 8   Isosurfaces of velocity perturbation relative to the laminar flow at $z = 0$ ($u' = \pm 0.1 U_\infty$ with dark surfaces for positive and light surfaces for negative perturbations): a) Hot3B, b) Cold3C, and c) Hot6C.
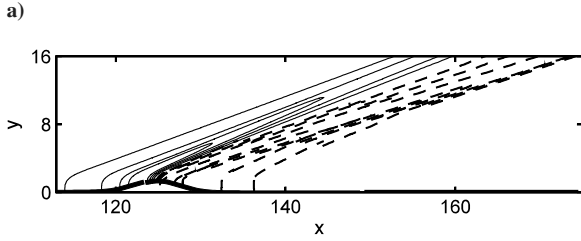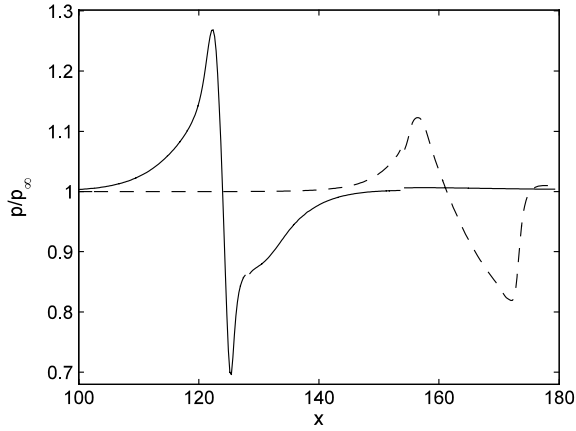
a)

b)

Fig. 9 Hot3B pressure normalized by the freestream value (p/p_∞): a) at the wall (solid line) and top of the domain (dashed line), b) contour of p/p_∞ at $z = 32$ (dashed lines are $p/p_\infty < 1$ and solid lines are $p/p_\infty > 1$ in increments of 5×10^{-2}).

produces local separated flow regions, these are small in extent and are evidently insufficient to lead to global instability of the wake behind the roughness element. Furthermore, the trends shown in Fig. 16 do not indicate that separation lengths are very sensitive in the main flow parameters, at least in the range studied here.

The frequency content of the shear layer before breakdown is measured by placing a virtual probe within the flow and computing the energy spectrum of the density fluctuations. Figure 17 shows the frequencies corresponding to a clear peak in the spectrum, plotted in the form of a Strouhal number $Sr = f\delta_h^*/U_h$. Because of the limited number of forcing frequencies and probe locations it is possible that in some cases the peak frequency identified is subject to a large error (especially at low frequencies) and the data needs to be treated with some caution. In all cases a similar trend to incompressible experiments [4–6] is shown, where Sr increases with Re_h. In case Hot6A all the forced modes are damped, and the lowest forced frequency is marked in Fig. 17 because it is decaying at the slowest
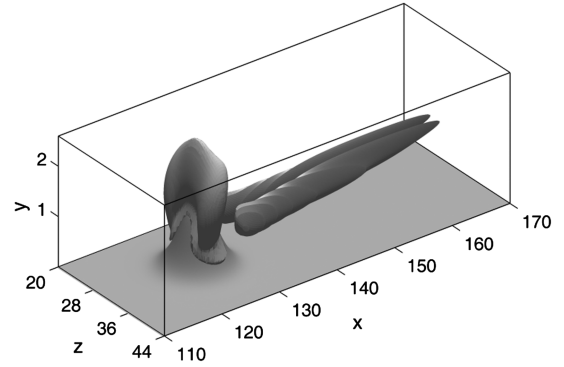

Fig. 11 Hot3B isosurfaces of $\Pi = -5 \times 10^{-3}$, without acoustic source. The y axis is stretched by a factor of 8.

rate. A general observation is that the values of Sr are lower than the incompressible measurements probably as a consequence of the high convective Mach number which shifts the most unstable wave to lower wavenumbers and frequencies [24].

With acoustic forcing, the perturbations are amplified and the shear layer breaks down (see Fig. 6). The lateral shear plays a role because the disturbances also appear in regions alongside the detached shear layer, forming the legs of hairpin-shaped structures. These structures pass downstream causing the flow to become increasingly chaotic and eventually to breakdown to turbulence. Sometimes the original hairpin structures are quite resilient and remain well into the region where the flow is turbulent. Figure 18 shows a plan view of a surface of constant Π and Fig. 18a is for the spanwise-symmetric acoustic forcing from Eq. (15) while Fig. 18b is for an asymmetrically forced case, which may trigger a separate mode of breakdown [11,23]. Both cases show the initial stages of breakdown to turbulence. In the symmetric case, hairpin vortices form with the heads originating in the detached shear and the legs from the lateral shear layers. In the asymmetric case, one-legged hairpin structures form but the final breakdown is at a similar location. In the remaining comparisons we consider only the symmetric mode of breakdown.

IV. Critical Roughness Height Reynolds Number

A number of simulations with widely varying conditions have been presented in this article and using all the results it is possible to look for correlations with the main flow parameters. In practical situations it is important to know whether transition is likely for a given roughness distribution in a known laminar boundary layer. Here we have only considered isolated smooth elements which may
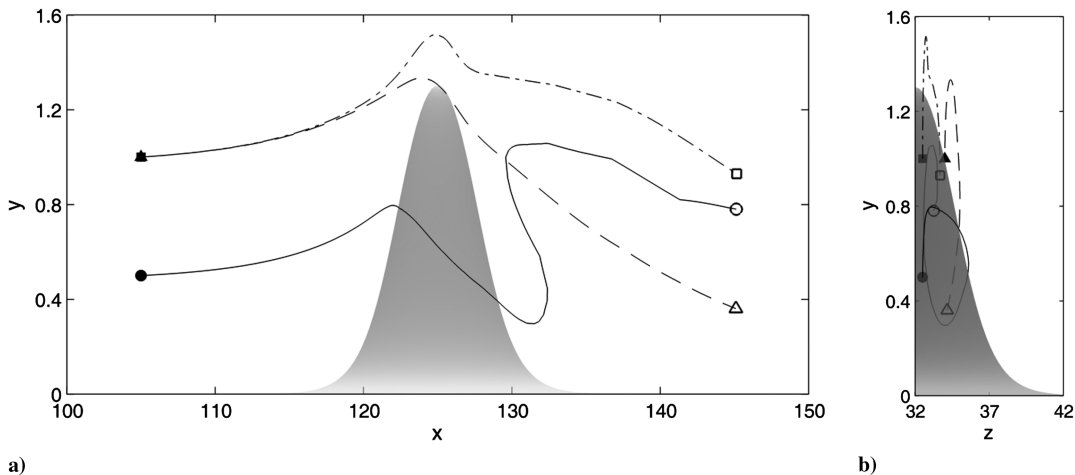

a)

b)

Fig. 10 Particle paths from case Hot3B (see Table 4): a) side view and b) front view calculated from a single velocity field. All particles starting at streamwise location $x = 105$ where there are filled symbols at $(y, z) = (0.5, 32.5)$ ——, $(y, z) = (1, 32.5)$ –·–, $(y, z) = (1, 34)$ – –. The end of a particle path is marked by an open symbol and the bump is made transparent so that the line behind it can be seen. The y axis is stretched by a factor of 16 relative to x and z.
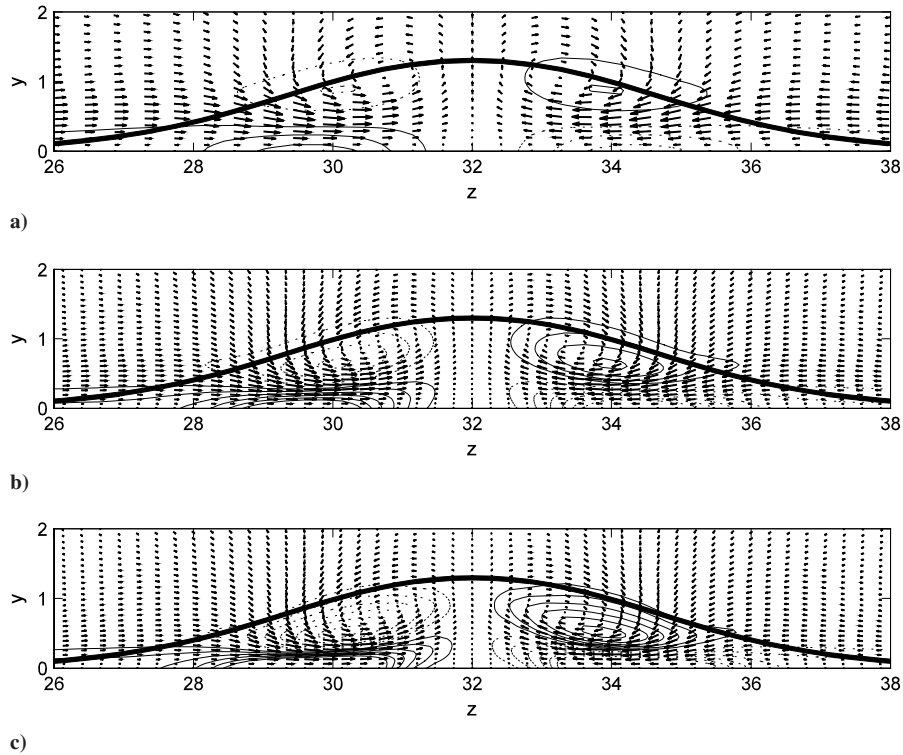
Fig. 12 Contours of streamwise vorticity (lines) with velocity vectors (arrows) at $x = 135$ for the Mach 3 hot wall cases: a) Hot3A $Re_h = 310$, b) Hot3B $Re_h = 592$, and c) Hot3C $Re_h = 920$. The contours are in increments of $\omega_x = 0.05$ and positive contours are solid lines while the dotted lines are negative. The streamwise direction is into the page.

or may not be representative of the transition process in practical applications. Nevertheless it is appropriate to consider the gross effects of changing the Mach number and thermal wall condition.

To correlate the results it is best to use parameters that can easily be defined, such as freestream quantities along with the roughness height Reynolds number (recall that $Re_h > 300$ is a condition for transition in low-speed flows). It needs to be noted that some of the high Mach number simulations reported here (Table 4) are at high Re_h but do not pass through transition. Furthermore, cases with the same Mach number and Re_h have different behavior depending on wall temperature. Thus any criterion for transition has to take into account at least Re_h, M, and T_w, and it seems more likely that the Mach number at the roughness height has more relevance than the freestream Mach number. On Fig. 19 we plot one combination of these parameters with which we have been able to separate laminar from transitional cases for all the simulations shown on Table 4. The figure shows the quantity M_h/T_w plotted against Re_h. Cases for which no transition was observed are shown with open symbols,
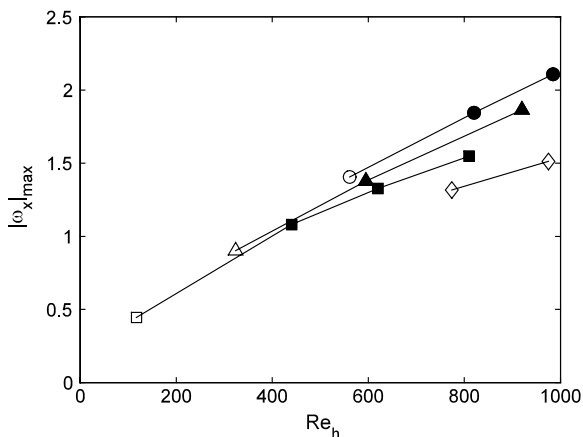
while cases that did undergo transition are shown with closed symbols. The solid line $M_h/T_w = 3(Re_h - 300)/700$ separates the laminar and transitional cases and reduces to the expected value for incompressible flow. Clearly more data (experimental and numerical) are needed to define the suitability of the parameter combinations and the shape of the dividing line at high M and low T_w (for example, the dividing line may well be flatter at high Re_h). Nevertheless, the success for the limited data available suggests that such a correlation is possible, at least for simple roughness shapes. The dividing line is also dependent upon the level of disturbances; lower background noise levels will move the line to the right. To check the effect of disturbance level, an additional simulation of Case Hot3B was run with half the forcing amplitude. The resulting skin-friction variation is shown on Fig. 20 and compared with the original result. We can see that the factor of 2 decrease in amplitude leads to a

Fig. 13 Peak streamwise vorticity: Hot3 $\triangle$, Cold3 $\bigcirc$, Hot6 $\square$, and Cold6 $\diamond$; filled symbols are cases that undergo transition.
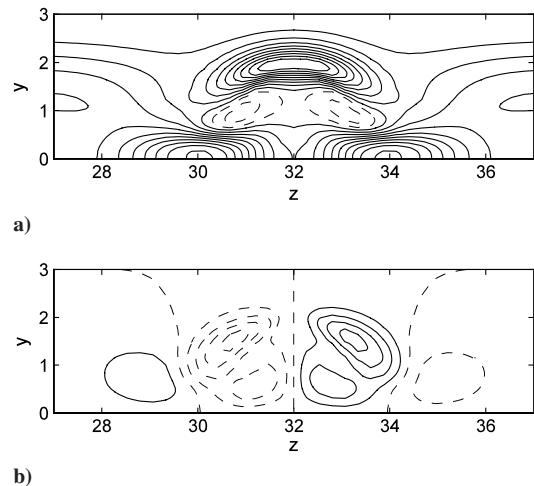

Fig. 14 Contours of $\partial u/\partial y$: a) and $\partial u/\partial z$ (b) for case Hot3B with acoustic forcing at $x = 155$. Contours increase in increments 0.125 with zero and below as dashed lines.
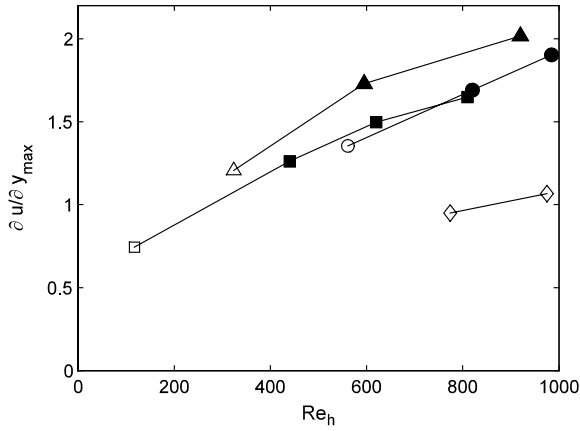
Fig. 15   Maximum $\partial u/\partial y$ in upper shear layer just before breakdown, Hot3 △, Cold3 ○, Hot6 □, and Cold6 ◇; filled symbols are transitional.

a)

b)

Fig. 18   Top view of a surface of $\Pi = -5 \times 10^{-3}$ for case Hot3B with: a) two-dimensional forcing, and b) three-dimensional forcing.
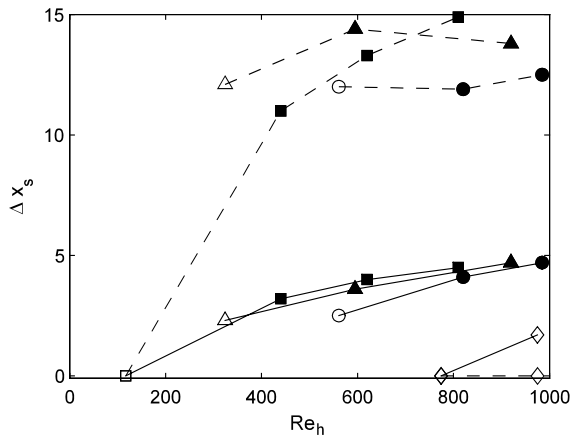

Fig. 16   Separation lengths at the front —— and rear – – of the bump measured along the domain centerline. Hot3 △, Cold3 ○, Hot6 □, and Cold6 ◇; filled symbols are transitional.

Fig. 19   Occurrence of transition in each case, Hot3 △, Cold3 ○, Hot6 □, and Cold6 ◇. Cases with transition to turbulence are shown with filled symbols. The dividing line is given by $M_h T_\infty/T_w = 3(Re_h - 300)/700$.

delay in streamwise location of the skin-friction rise of about 10 (normalized with δ_0^*), which compares to the normalized transition length for this case of 70 (i.e., a 14% change). The dependence is relatively small due to the exponential growth rates of the detached shear layer instability.

Even when the transitional cases are separated from the laminar cases, we do not yet have a prediction of transition point. Defining x_t as the point at which the skin-friction coefficient starts to rise rapidly toward the turbulent value (for example $x_t \approx 180$ on Fig. 7), Fig. 21
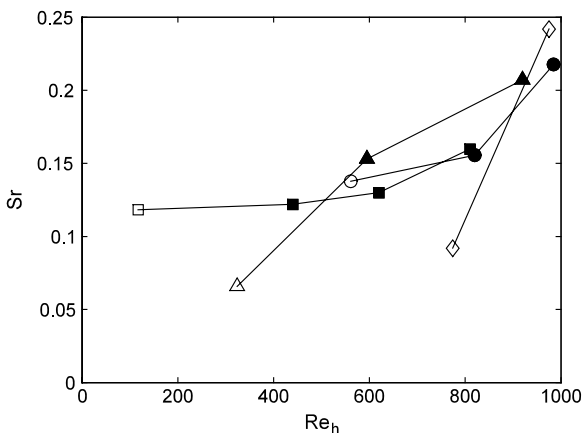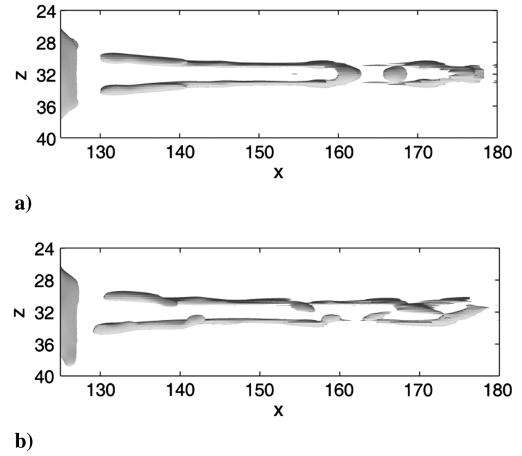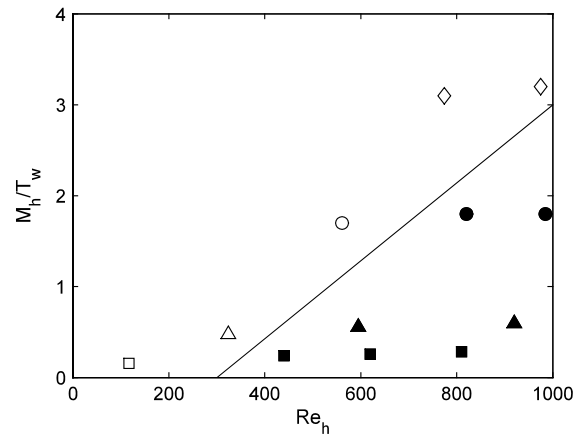
shows an inverse transition length plotted against Re_h (with this method, simulations that gave no transition are marked with a data point on the horizontal axis). We can see that there is an increasing trend to the curves, showing a decreasing transition distance as Re_h is increased. There is also a Mach number and wall temperature effect giving a wide spread to the data points, which could be explained by
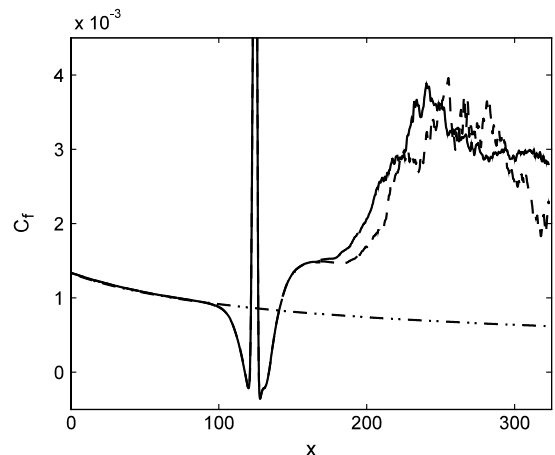

Fig. 17   Measured shear layer Strouhal numbers for selected cases: Hot3 △, Cold3 ○, Hot6 □, and Cold6 ◇; filled symbols are transitional.

Fig. 20   The effect of acoustic forcing on flow with roughness. Case Hot3B, —— with standard forcing [$a_f = 1/80$, see Eq. (15)], – – – with half amplitude forcing ($a_f = 1/160$), — · · — is the laminar flow correlation of Eckert [20].
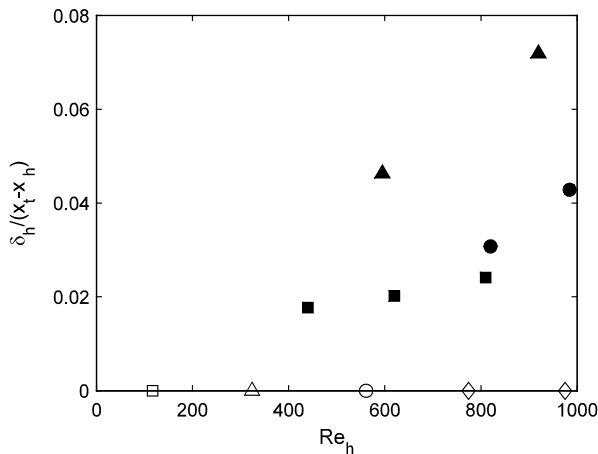
Fig. 21 Inverse transition length Hot3 $\triangle$, Cold3 $\bigcirc$, Hot6 $\square$, and Cold6 $\diamondsuit$. Filled symbols are transitional and cases without transition appear on the lower horizontal axis.

the measurements of convective Mach number which increase with transition length (see Sec. III.B). Given the limited available data no attempt was made to collapse these data points. It would be interesting in the future to compare the present results with transient growth analysis (e.g., [25]). Additionally, new experimental data are starting to appear (e.g., [26]) for cylindrical roughness elements with larger roughness Reynolds numbers than those considered here) and it should be feasible using experiment and simulation to develop a much more complete coverage of the large parameter space for roughness-induced transition in high-speed flows.

V.   Conclusions

Transition due to roughness in high-speed boundary layers is more complicated than in low-speed flows, with the Mach number and thermal wall boundary condition playing a significant role, in addition to the roughness height Reynolds number. Nevertheless many features of the transition process are similar to low-speed flow, in particular the lift-up process that follows the formation of streamwise vortices as the flow passes over the roughness element. The lift-up forms detached shear layers, again following a well understood mechanism, and this shear layer is unstable. The initial vorticity level found behind the roughness element was found to be dependent mainly on the roughness height Reynolds number. It was found that acoustic disturbances were more efficient at stimulating the shear layer instability compared with upstream boundary-layer disturbances, perhaps because the boundary layer near the roughness element is particularly receptive to external disturbances.

The occurrence or otherwise of transition was found to depend on Mach number, wall temperature, and Reynolds number, and a particular combination of these parameters was shown to separate laminar from transitional flow for the range of parameters studied here. Transition is delayed to higher Reynolds numbers as the Mach number increases and as the wall is cooled. The present work has clearly demonstrated the feasibility of direct numerical simulation to study transition over isolated roughness elements under a controlled environment. More experiments and simulations in the future are needed to extend the present parameter range, for example for different heights and shapes of roughness elements and different disturbance fields.

References

[1]   Reshotko, E., "Transition Issues for Atmospheric Entry," *Journal of Spacecraft and Rockets*, Vol. 45, No. 2, 2008, pp. 161–164.
      doi:10.2514/1.29777
[2]   Schneider, S. P., "Effects of Roughness on Hypersonic Boundary-Layer Transition," *Journal of Spacecraft and Rockets*, Vol. 45, No. 2, 2008, pp. 193–209.
      doi:10.2514/1.29713
[3]   Tani, I., "Boundary-Layer Transition," *Annual Review of Fluid Mechanics*, Vol. 1, 1969, pp. 169–196.
      doi:10.1146/annurev.fl.01.010169.001125
[4]   Klebanoff, P. S., Cleveland, W. G., and Tidstrom, K. D., "On the Evolution of a Turbulent Boundary Layer Induced by a Three-Dimensional Roughness Element," *Journal of Fluid Mechanics*, Vol. 237, 1992, pp. 101–187.
      doi:10.1017/S0022112092003379
[5]   Ergin, F. G., and White, E. B., "Unsteady and Transitional Flows Behind Roughness Elements," *AIAA Journal*, Vol. 44, No. 11, 2006, pp. 2504–2514.
      doi:10.2514/1.17459
[6]   Acarlar, M. S., and Smith, C. R., "A Study of Hairpin Vortices in a Laminar Boundary Layer. Part 1. Hairpin Vortices Generated by a Hemispherical Protuberance," *Journal of Fluid Mechanics*, Vol. 175, 1987, pp. 1–41.
      doi:10.1017/S0022112087000272
[7]   Rizzetta, D. P., and Visbal, M. R., "Direct Numerical Simulations of Flow Past an Array of Distributed Roughness Elements," *AIAA Journal*, Vol. 45, No. 8, 2007, pp. 1967–1976.
      doi:10.2514/1.25916
[8]   Holloway, P. F., and Sterrett, J. R., "Effect of Controlled Surface Roughness on Boundary-Layer Transition and Heat Transfer at Mach Numbers of 4.8 and 6.0," NASA TN D-2054, 1964.
[9]   Balakumar, P., "Receptivity of a Supersonic Boundary Layer to Acoustic Disturbances," *AIAA Journal*, Vol. 47, No. 5, 2009, pp. 1069–1078.
      doi:10.2514/1.33395
[10] Marxen, O., and Iaccarino, G., "Numerical Simulation if the Effect of a Roughness Element on High-Speed Boundary-Layer Instability," *38th Fluid Dynamics Conference and Exhibit*, AIAA Paper 2008-4400, Seattle, WA, June 2008.
[11] Groskopf, G., Kloker, M. J., and Marxen, O., "Bi-global Crossplane Stability Analysis of High-Speed Boundary-Layer Flows with Discrete Roughness," *Seventh IUTAM Symposium on Laminar-Turbulent Transition*, Springer, New York, June 2009.
[12] Piot, E., Casalis, G., and Rist, U., "Stability of the Laminar Boundary Layer Flow Encountering a Row of Roughness Elements: Biglobal Stability Approach and DNS," *European Journal of Mechanics B: Fluids*, Vol. 27, No. 6, 2008, pp. 684–706.
      doi:10.1016/j.euromechflu.2008.01.007
[13] Fischer, M. C., "Spreading of a Turbulent Disturbance," *AIAA Journal*, Vol. 10, No. 7, 1972, pp. 957–959.
      doi:10.2514/3.50265
[14] Krishnan, L., and Sandham, N. D., "Effect of Mach number on the Structure of Turbulent Spots," *Journal of Fluid Mechanics*, Vol. 566, 2006, pp. 225–234.
      doi:10.1017/S0022112006002412
[15] Redford, J. A., Sandham, N. D., and Roberts, G. T., "Parametric Study of Compressible Turbulent Spots," *Seventh International ERCOFTAC Workshop on Direct and Large-Eddy Simulation*, Springer, New York, 2008, pp. 177–178.
[16] Yee, H. C., Sandham, N. D., and Djomeri, M., "Low-Dissipative High-Order Shock-Capturing Methods using Characteristic Based Filters," *Journal of Computational Physics*, Vol. 150, No. 1, 1999, pp. 199–238.
      doi:10.1006/jcph.1998.6177
[17] Sandham, N. D., Li, Q., and Yee, H., "Entropy Splitting for Higher-Order Numerical Simulation of Compressible Flow," *Journal of Computational Physics*, Vol. 178, No. 2, 2002, pp. 307–322.
      doi:10.1006/jcph.2002.7022
[18] Anderson, J. D., *Computational Fluid Dynamics*, McGraw–Hill, New York, 1995.
[19] Sandham, N. D., and Lüdeke, H., "A Numerical Study of Mach 6 Boundary Layer Stabilization by means of a Porous Surface," *47th AIAA Aerospace Sciences Meeting*, AIAA Paper 2009-1288, Jan. 2009, Orlando, FL.
[20] Eckert, E. R. G., "Engineering Relations for Friction and Heat Transfer to Surfaces in High Velocity Flow," *Journal of Aerospace Sciences*, Vol. 22, No. 8, 1955, pp. 585–587.

[21] Stuart, J. T., "The Production of Intense Shear Layers by Vortex Stretching and Convection," AGARD R-514, May 1965.

[22] Sandham, N. D., and Kleiser, L., "The Late Stages of Transition to Turbulence in Channel Flow," *Journal of Fluid Mechanics*, Vol. 245, 1992, pp. 319–348.
doi:10.1017/S002211209200048X

[23] Andersson, P., Brandt, L., Bottaro, A., and Henningson, D. S., "On the Breakdown of Boundary Layer Streaks," *Journal of Fluid Mechanics*, Vol. 428, 2001, pp. 29–60.
doi:10.1017/S0022112000002421

[24] Sandham, N. D., and Reynolds, W. C., "Compressible Mixing Layer: Linear Theory and Direct Simulation," *AIAA Journal*, Vol. 28, No. 4, 1990, pp. 618–624.
doi:10.2514/3.10437

[25] Reshotko, E., and Tumin, A., "Role of Transient Growth in Roughness-Induced Transition," *AIAA Journal*, Vol. 42, No. 4, 2004, pp. 766–770.
doi:10.2514/1.9558

[26] Danehy, P. M., Ivey, C. B., and Inman, J. A., "High Speed PLIF Imaging of Hypersonic Transition over Discrete Roughnesses," AIAA Paper 2010-0703.

S. Fu
Associate Editor